Three-dimensional nonlinear optical holograms

Yujia Wu,[1] Haigang Liu,[1,*] and Xianfeng Chen [1,2,3,†]

[1]*State Key Laboratory of Advanced Optical Communication Systems and Networks, School of Physics and Astronomy, Shanghai Jiao Tong University, Shanghai 200240, China*

[2]*Collaborative Innovation Center of Light Manipulations and Applications, Shandong Normal University, Jinan 250358, China*

[3]*Jinan Institute of Quantum Technology, Jinan 250101, China*

The three-dimensional holography technique offers an efficient and convenient tool for storing depth information of the object and provides more realistic images compared to the two-dimensional case, which has been widely used in the fields of optical tweezers, image encryption, and optical microscopy. However, such a three-dimensional nonlinear holography technique is still lacking in the field of nonlinear optics. Here, we demonstrate the realization of three-dimensional nonlinear optical holograms. Without loss of generality, a second-order nonlinearity is used in our experiment and the generated second harmonic with multiplane patterns at different depths is dynamically realized. This study opens up the field of three-dimensional spatial nonlinear harmonic manipulation and may have applications in all-optical wave-band three-dimensional optical imaging, parallel micromachining, holographic displays, and so on.

The holography technique can be used to reconstruct the amplitude and phase information of an object by introducing coherent interference of the reference and object wave in the recorded medium. Since it was realized by Gabor in 1948 [1], such a holography technique has been developed in many fields where the wave exists, including electron [2–4], x-ray [5–7], and wireless holography [8], optics [9–14], and surface plasmon polaritons [15]. In the field of optics, such a holography technique became available after the invention of the laser and now it is widely used in microscopy [9,10], optical tweezing [11,12], quantum information [13,14], and so on [16,17]. We know that as more information can be reconstructed by the holography technique, the images become more vivid compared to the objects in the real world. Therefore, all kinds of holography techniques have been proposed in the development process, such as three-dimensional (3D) holograms [18,19], polarization holograms [20,21], and color holograms [22], to infinite approximations of real objects in the natural world. Among them, the 3D holography technique has attracted considerable public interest especially in the field of holographic 3D displays [19,23,24], because the images can be seen with the unassisted eye from different angles and it is very similar to how humans see the actual environment surrounding them.

As we know, such a holography realization is sensitive to the wavelength of the holography material. In most situations, researchers are eager for an all-optical wave-band realization of the holography technique for use in different fields, such as photoetching [25–27] and holography displays [28,29]. One method to circumvent this problem is

to develop the holography material, which satisfies different wave-band requirements [28,29]. However, this method needs to redesign the structure of the holography material with the changing of the laser wavelength and it is also hard to extend the wavelength scope of the holography realization once the holography material is determined. Nonlinear frequency conversion as a common method to extend the wavelength scope is naturally another way to realize this assignment. In recent years, nonlinear holography has been introduced into nonlinear optics assisted by the microstructure of nonlinear photonic crystals (NPCs), which were used to realize nonlinear harmonic wave-front shaping [30,31]. In such nonlinear frequency conversion processes, the conversion efficiency always needs to be considered. Therefore, such a nonlinear hologram concept was first realized along the quasi-phase-matching (QPM) direction in a one-dimensional (1D) manner, which maximizes the conversion efficiency as much as possible [32]. Although the depth information is considered in the nonlinear volume holography process, some of the 1D information along the transverse direction of the NPCs is missed for the sake of a high nonlinear conversion efficiency. In addition, two-dimensional (2D) holography information can be reconstructed by losing sight of the nonlinear conversion efficiency problem because of the intrinsic limitation of the NPCs [33,34]. Recently, the 3D modulation of the nonlinear coefficient has been realized, which is still used to realize 2D shaping [35,36]. The problems of this method are also the complex fabrication of NPCs and lack of flexibility, which seriously influence its applications in actual situations. To overcome these limitations of the method to manipulate the microstructure of NPCs, dynamic nonlinear optical holograms where the structure property puts on the incident light have been further developed in our previous research [37,38]. Arbitrary special beams or patterns in both fundamental-

---

*liuhaigang@sjtu.edu.cn

†xfchen@sjtu.edu.cn

frequency and second-harmonic (SH) wave bands can be dynamically generated at the same time. Until now, only 2D information of the nonlinear harmonic waves has been generated and manipulated in all kinds of nonlinear holography processes mentioned above. Therefore, real 3D holography has yet to be explored in the nonlinear optical process.

In this article, we report 3D nonlinear optical holograms, which have a high nonlinear conversion efficiency and a dynamic property at the same time. To demonstrate its feasibility, the two-turn hollow helix pattern is well reconstructed in four imaging planes at first in our experiment. Next, the simple letters of "X," "Y," and "Z" are also well reconstructed in three imaging planes. To analyze the reconstruction results, the mean-square errors (MSEs) of the reconstructed images are calculated by comparing with the random noise images of MSE_0. Furthermore, SH patterns of a bird and rabbit in different depths can be successfully reconstructed to further demonstrate its ability to be applied in complex situations. The dynamic property is quite important to realize the real sense of the 3D nonlinear hologram display and can significantly increase its flexibility. Therefore, we show a dynamic SH elephant and cat in a multiplane as the last experiment because the fundamental-frequency wave (FW) can be dynamically controlled by the spatial light modulator (SLM) in our method. In addition, we also calculate the normalized nonlinear conversion efficiency.

In a nonlinear optical hologram, the nonlinear polarization wave $E_{NPW}(2\omega) = [\frac{\chi^{(2)}}{\chi^{(1)}}]E_{FW_1}(\omega)E_{FW_2}(\omega)$ is treated as the reference beam to interfere with the SH wave (SHW). Here, $\chi^{(1)}$ and $\chi^{(2)}$ are the linear and the second-order nonlinear optical susceptibilities, respectively. $E_{FW_1}(\omega)$ and $E_{FW_2}(\omega)$ are the incident FWs, which can form a dynamic grating in a nonlinear crystal. According to the theoretical analysis of our previous work [38], the structure function of the FW can be expressed as

$$f(\xi, \eta, \kappa) = E_{SHW}^* E_{NPW} + E_{SHW} E_{NPW}^*. \quad (1)$$

In order to get the SH pattern in the far field, the Fourier electric field of the object is recorded. The transform relation between the far field and near field in a 3D hologram can be represented as

$$A(x, y, z) = \sum_{i=1}^{m} \left\{ \exp\left[-j\frac{\pi}{\lambda_{SH}f^2}\left(1 - \frac{d_i}{f^2}\right)(x^2 + y^2) \right] \right\}$$
$$\times \mathcal{F}\{A(\xi, \eta, \kappa)\}_{f_x = \frac{x}{\lambda_{SH}z}, f_y = \frac{y}{\lambda_{SH}z}}, \quad (2)$$

where $A(x, y, z)$ and $A(\xi, \eta, \kappa)$ are, respectively, the amplitudes of SH at the planes of 3D screens and Σ, as shown in Fig. 1. x, y, z and ξ, η, κ represent the coordinate systems of the plane of 3D screens and Σ, respectively. f is the focal distance of the lens and λ_{SH} is the wavelength of the SHW. f_x and f_y are, respectively, the spatial frequency of the SHW along the x and y directions. m is the number of imaging layers of such a 3D nonlinear hologram. d_i is the distance between the ith imaging plane and the Fourier lens plane.

Figure 2 shows the experimental setup for the reconstruction of such a 3D nonlinear object. An Nd:YAG nanosecond laser with 1064 nm wavelength and 20 Hz repetition rate is used as the FW pump source, which produces 4 ns pulses. A
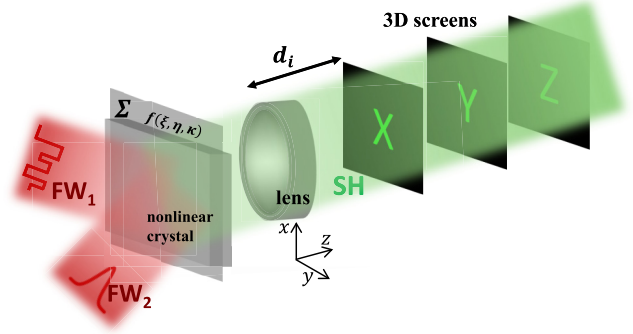

FIG. 1. Schematic of realizing 3D nonlinear holography. Σ is the plane of the nonlinear interaction in a nonlinear crystal, and $f(\xi, \eta, \kappa)$ represents the structure function. The lens is used to image at different depth positions.

half-wave plate (HWP) and a Glan-Taylor prism (GTP) are used to control the polarization and intensity of the FW. After being collimated and expanded by the lenses L_1 ($f_1 = 30$ mm) and L_2 ($f_2 = 100$ mm), the vertically polarized laser is incident onto a SLM, which is used to control the arbitrary phase structure of the FW. The SLM has a resolution of 512×512 pixels, each with a rectangular area of 19.5×19.5 μm^2. We use a 4-f system consisting of L_3 ($f_3 = 200$ mm) and L_4 ($f_4 = 50$ mm) to imprint the modulated wave-front pattern of the FW onto the onset of the nonlinear crystal. We filter out undesired FWs by a spatial filter (SF) between L_3 and L_4. The object wave $E_{FW_1}(\omega) = A_1 \exp(-2j\pi\alpha z) \exp[-i\phi(x, y)]$ and Gaussian pump wave $E_{FW_2}(\omega) = A_2 \exp[-(x^2 + y^2)/\omega_0^2]$ are incident into the nonlinear crystal, where A_1 and A_2 are, respectively, the amplitude of the object wave and Gaussian pump wave. α is the angle between these two FWs, ω_0 is the Gaussian wave waist, and $\phi(x, y)$ is the phase structure of the FWs. In our experiment, 5 mol % MgO:LiNbO$_3$ (LN) is used to realize the nonlinear frequency conversion and cut for the noncollinear SH generation process. In order to satisfy birefringent phase matching, the LN is cut along the direction of $75°$ with respect to the c axis of the crystal according to the Sellmeier equation [39]. The FWs are o polarized and the generated SH is e polarized. After LN, the lens L_5 ($f_5 = 200$ mm) is used to image each layer of object information by
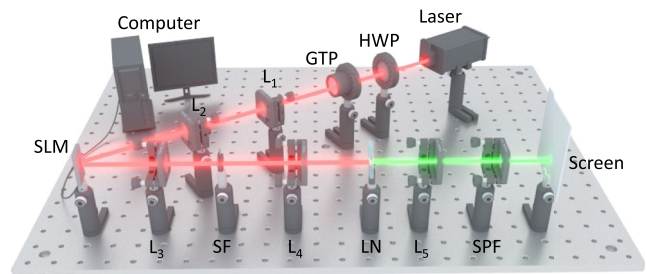

FIG. 2. Schematic of the experimental setup to implement a 3D nonlinear hologram (see text for details). HWP: half-wave plate; GTP: Glan-Taylor prism; SLM: spatial light modulator; SF: spatial filter; LN: 5 mol % MgO:LiNbO$_3$; SPF: short-pass filter; L_{1-5}: lens, $f_{1-5} = 30, 100, 200, 50,$ and 200 mm, respectively.
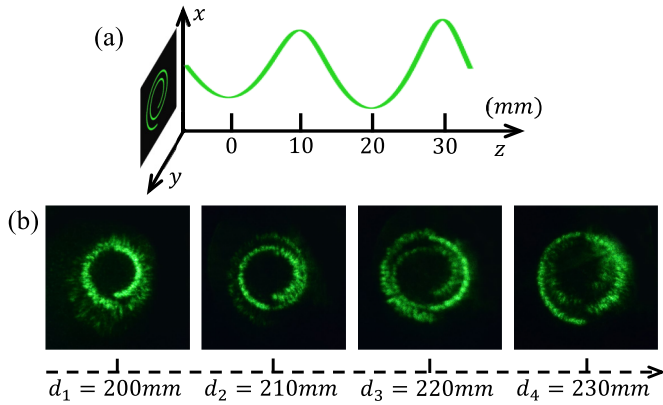
FIG. 3. (a) Geometry of the helix. (b) Experimentally reconstructed SH patterns on different 2D planes along the z-axis direction.
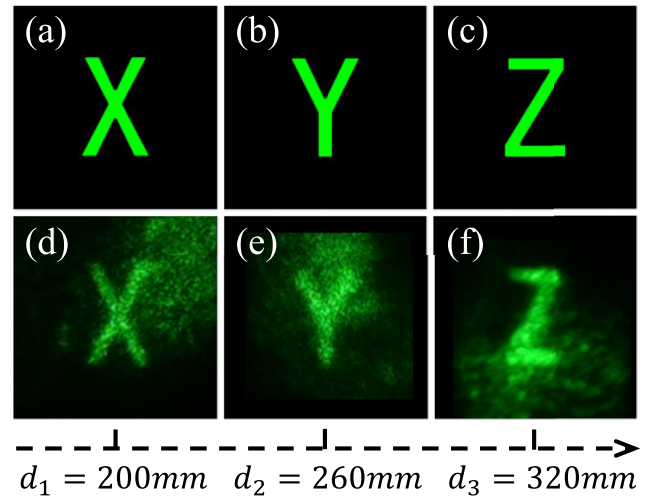

FIG. 4. (a)–(c) show the profiles of the desired SH patterns corresponding to letters X, Y, and Z, respectively. (d)–(f) are the experimentally reconstructed SH patterns in their own imaging planes.

a Fourier transform. Finally, we filter out the infrared FWs by the short-pass filter (SPF) and use a camera to capture the 3D image at different depths along the z-axis direction.

First, the 3D spatial variation SH patterns are reconstructed in the experiment. As shown in Fig. 3(a), the original 3D object is a two-turn hollow helix pattern with a 10-mm pitch along the z-axis direction. By tuning the imaging plane, the reconstruction of the 3D helix image on four 2D planes is measured at different distances, as shown in Fig. 3(b). Only the inner half of the helix can be clearly reconstructed when $d_1 = 200$ mm, while other parts of the helix are out of focus and appear blurry. With an increase of the z-axis distance, each middle part of the helix can form sharp images, as shown by the experimental results when $d_2 = 210$ mm and $d_3 = 220$ mm. Finally, the top part is well imaged at $d_4 = 230$ mm. As a result, the 3D nonlinear holographic image of the helix pattern has been successfully reconstructed.

In addition to the simple lines in the 3D space, the 3D nonlinear optical hologram can also be designed to reconstruct simple SH letters in different planes. The desired SH patterns corresponding to the letters X, Y, and Z are, respectively, shown in Figs. 4(a)–4(c), and the experimental reconstruction results are shown in Figs. 4(d)–4(f). The depth positions of the reconstructed SH letters are 200, 260, and 320 mm, respectively. We would like to point out that weak speckle noise can be observed due to the mutual disturbance of the SH in different imaging planes although the 3D information is well reconstructed in the experiment.

In order to quantitatively analyze the reconstruction results of our 3D nonlinear holography, the MSE is commonly introduced. It is an average of the squares of the difference between the experimental pixel values and the theoretical pixel values of images, which can be represented as

$$\text{MSE} = \frac{\sum_{m,n} [I(m, n) - I_0(m, n)]^2}{M \times N}, \quad (3)$$

where M and N are the number of pixels of SLM along the horizontal and vertical directions. $I(m, n)$ and $I_0(m, n)$ represent the optical intensity matrices of experimental results and original images. The summation $\sum_{m,n}$ is over all possible pixels with index (m, n) of the image. A low MSE generally indicates a high-quality reconstruction. We calculate

the MSE between the reconstructed and original images. For comparison, random noise images are adopted to calculate the same quantities MSE_0 in which the matrices $I(m, n)$ are replaced by random numbers. The results of MSE and MSE_0 are shown in Table I. It is clear to see that the values of MSE of the reconstructed images are an order of magnitude smaller than the random noise images. In other words, the images can be well reconstructed by using the 3D nonlinear holography technique proposed here.

The disturbance between different imaging planes will be more serious when complex SH patterns are reconstructed. Therefore, we choose a two-plane system here to illustrate the reconstruction ability of the complex objects. The profiles of the desired more complex SH patterns of a bird and rabbit are shown in Figs. 5(a) and 5(b) and the experimental results are shown in Figs. 5(c) and 5(d), which are formed at planes of 200 and 230 mm. For these two results, the MSE_0 between random noise and the original images is 0.3203 and 0.3183, respectively. The corresponding values of the MSEs are 0.0384 and 0.0529, which indicates the experimental results are also in good agreement with the desired amplitude patterns.

Furthermore, the dynamic property is also extremely important for all-optical wave-band 3D holographic displays and can significantly increase the flexibility when it is used in different areas. Fortunately, the structure property of Eq. (1) in our method is provided by two FWs which can be tuned dynamically by SLM. In our experiment, the dynamic video of the complex nonlinear images is realized in the 3D case, where a walking elephant and a wagging tail cat including

TABLE I. The results of MSE and MSE_0.

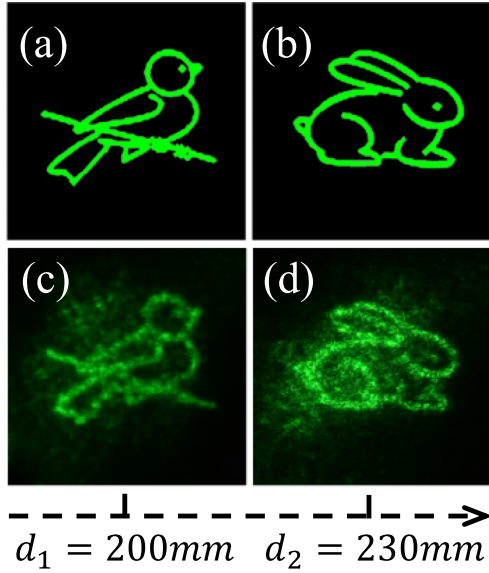|	Letter X	Letter Y	Letter Z
MSE	0.0154	0.0121	0.0155
MSE_0	0.3292	0.3303	0.3287

$$d_1 = 200mm \quad d_2 = 230mm$$

FIG. 5. (a) and (b) show the profiles of the desired more complex SH patterns of a bird and rabbit. (c) and (d) are the corresponding experimentally reconstructed SH patterns in their own imaging planes.

eight typical frames are reconstructed. The first and third rows of Fig. 6 are the desired profiles of the SH patterns for a walking elephant and a wagging tail cat, respectively. Only the odd frames of the SH patterns are shown here and the experimental results are shown in the second and fourth rows of Fig. 6. The walking elephant and wagging tail cat are at a distance of $d_1 = 300$ mm and $d_2 = 330$ mm. In our
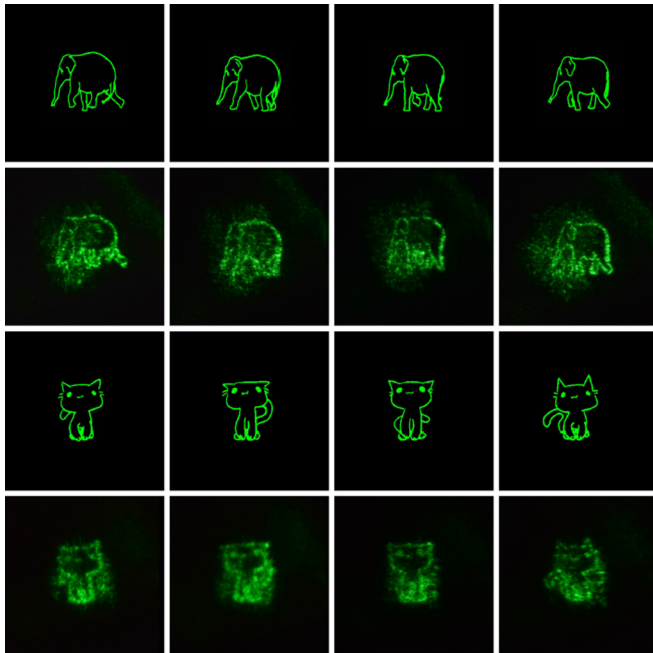

FIG. 6. The first and third row are the profiles of the desired SH patterns for a walking elephant and a wagging tail cat. The second and fourth rows are the experimental observations corresponding to the first and third rows. Complete videos of the dynamic images are shown in Movie 1 in the Supplemental Material [40].
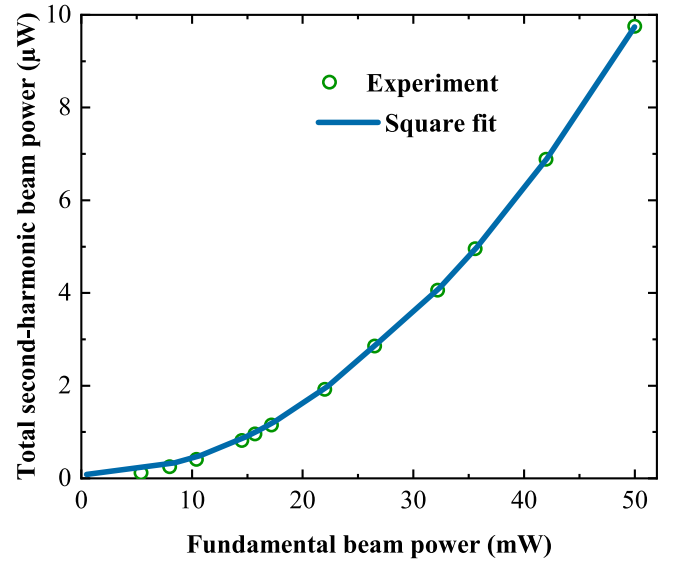

FIG. 7. Comparison between measured (circle) and square fit (solid curves) results of the average SH beam power dependence on the average FW input power.

experiment, the refresh rate of SLM is 1 Hz and it can be tuned up to 60 Hz, which depends on the SLM. A complete movie of the dynamic images is shown in the Supplemental Material [40].

In our experiment, the SH beam power $P_{2\omega}$ varying with the power of the FW P_ω is shown in Fig. 7. The normalized conversion efficiency η_{nor} of the SH is given by

$$\eta_{\text{nor}} = \frac{P_{2\omega}}{P_\omega^2 L^2}, \qquad (4)$$

where L is the length of the nonlinear crystal [41]. Obviously, Fig. 7 confirms a well-known quadratic relation between the average power of the SH and FW. The normalized nonlinear conversion efficiency for the average power of a 1-mm-thick crystal is 39% $\text{W}^{-1}\,\text{cm}^{-2}$. We have also calculated the normalized conversion efficiency for peak power. The average input power of 50 mW corresponding to the input peak power is 625 kW. The average output SH power of 9.75 μW corresponding to the output SH peak power is 122 W. Therefore, the normalized conversion efficiency for peak power is $3 \times 10^{-6}\%\,\text{W}^{-1}\,\text{cm}^{-2}$. It should be noted that we calculate the theoretical normalized conversion efficiencies without considering the Fresnel losses. The conversion efficiency can be further improved by using a longer nonlinear crystal.

Only the linear process was studied in previous 3D holography works, therefore, their methods only covered a small range of wave bands that are determined by the property of the linear holography materials. We can generate 3D optical holograms in an arbitrary wave band by using different nonlinear frequency conversion processes in theory, such as the sum-frequency and difference-frequency processes, which can efficiently extend the wavelength scope of such 3D holography without redesigning the structure of the holography material. In addition, the dynamic property of our method can significantly increase flexibility when such nonlinear 3D holograms are used in different areas. We also note that

the high spatial frequency information of the origin image may not be well reconstructed due to the limitation of the phase-matching angle in the nonlinear frequency conversion process. In fact, we adopt the paraxial approximation of the FW and the reconstructed results are not affected seriously according to our experimental results. This problem can be further overcome by utilizing a phase-matching condition with a broadband angle. In addition, the damage of SLM is relatively low and the modulation rate of SLM affects its high-speed modulation. In the future, a high damage threshold SLM and high-speed modulators such as a digital micromirror device (DMD) can be used.

In summary, we have proposed and experimentally demonstrated 3D nonlinear optical holograms in an SH generation process, which has a high nonlinear conversion efficiency and a dynamic property at the same time. In our experiment, SH patterns corresponding to the two-turn hollow helix, the letters X, Y, and Z, or a bird and rabbit can be well reconstructed simultaneously at different depths. The quality of the SH patterns has been analyzed, which demonstrates its reconstruction capability. The dynamic property is also manifested by the movie of a walking elephant and a wagging tail cat at different depth positions. This study opens up the field of 3D nonlinear harmonic manipulation and may have applications in all-optical wave-band 3D optical imaging, parallel micromachining, holographic displays, and so on.

[1] D. Gabor, A new microscopic principle, Nature (London) **161**, 777 (1948).

[2] H. Chen, Y. Chen, D. Dilworth, J. L. E. Leith, and J. Valdmanis, Two-dimensional imaging through diffusing media using 150-fs gated electronic holography techniques, Opt. Lett. **16**, 487 (1991).

[3] J. Cumings, A. Zettl, M. R. McCartney, and J. C. H. Spence, Electron Holography of Field-Emitting Carbon Nanotubes, Phys. Rev. Lett. **88**, 056804 (2002).

[4] H. Sasaki, K. Yamamoto, Y. Ichihashi, and T. Senoh, Image size scalable full-parallax coloured three-dimensional video by electronic holography, Sci. Rep. **4**, 4000 (2014).

[5] M. Tegze, G. Faigel, S. Marchesini, M. Belakhovsky, and O. Ulrich, Imaging light atoms by X-ray holography, Nature (London) **407**, 38 (2000).

[6] D. Gauthier, M. Guizar-Sicairos, X. Ge, W. Boutu, B. Carré, J. R. Fienup, and H. Merdji, Single-Shot Femtosecond X-Ray Holography using Extended References, Phys. Rev. Lett. **105**, 093901 (2010).

[7] J. Geilhufe, B. Pfau, M. Schneider, F. Büttner, C. M. Günther, S. Werner, S. Schaffert, E. Guehrs, S. Frömmel, M. Kläui, and S. Eisebitt, Monolithic focused reference beam X-ray holography, Nat. Commun. **5**, 1 (2014).

[8] S. Jivkova and M. Kavehrad, Holographic optical receiver front end for wireless infrared indoor communications, Appl. Opt. **40**, 2828 (2001).

[9] P. Marquet, B. Rappaz, P. J. Magistretti, E. Cuche, Y. Emery, T. Colomb, and D. Christian, Digital holographic microscopy: A noninvasive contrast imaging technique allowing quantitative visualization of living cells with subwavelength axial accuracy, Opt. Lett. **30**, 468 (2005).

[10] S. A. Alexandrov, T. R. Hillman, T. Gutzler, and D. D. Sampson, Synthetic Aperture Fourier Holographic Optical Microscopy, Phys. Rev. Lett. **97**, 168102 (2006).

[11] A. N. Grigorenko, N. W. Roberts, M. R. Dickinson, and Y. Zhang, Nanometric optical tweezers based on nanostructured substrates, Nat. Photonics **2**, 365 (2008).

[12] E. R. Dufresne, G. C. Spalding, M. T. Dearing, S. A. Sheets, and D. G. Grier, Computer-generated holographic optical tweezer arrays, Rev. Sci. Instrum. **72**, 1810 (2001).

[13] K. Tordrup, A. Negretti, and K. Mølmer, Holographic Quantum Computing, Phys. Rev. Lett. **101**, 040501 (2008).

[14] D. V. Vasilyev, I. V. Sokolov, and E. S. Polzik, Quantum memory for images: A quantum hologram, Phys. Rev. A **77**, 020302(R) (2008).

[15] J. Chen, T. Li, S. M. Wang, and S. N. Zhu, Multiplexed holograms by surface plasmon propagation and polarized scattering, Nano Lett. **17**, 5051 (2017).

[16] R. Di Leonardo, J. Leach, H. Mushfique, J. M. Cooper, G. Ruocco, and M. J. Padgett, Multipoint Holographic Optical Velocimetry in Microfluidic Systems, Phys. Rev. Lett. **96**, 134502 (2006).

[17] P. Genevet, J. Lin, M. A. Kats, and F. Capasso, Holographic detection of the orbital angular momentum of light with plasmonic photodiodes, Nat. Commun. **3**, 1 (2012).

[18] S. Kishk and B. Javidi, Watermarking of three-dimensional objects by digital holography, Opt. Lett. **28**, 167 (2003).

[19] S. Tay, P. A. Blanche, R. Voorakaranam, A. V. Tunç, W. Lin, S. Rokutanda, T. Gu, D. Flores, P. Wang, G. Li, P. St Hilaire, J. Thomas, R. A. Norwood, M. Yamamoto, and N. Peyghambarian, An updatable holographic three-dimensional display, Nature (London) **451**, 694 (2008).

[20] W. T. Chen, K. Y. Yang, C. M. Wang, Y. W. Huang, G. Sun, I. D. Chiang, C. Y. Liao, W. L. Hsu, H. T. Lin, S. Sun, L. Zhou, A. Q. Liu, and D. P. Tsai, High-efficiency broadband meta-hologram with polarization-controlled dual images, Nano Lett. **14**, 225 (2014).

[21] B. Wang, F. Dong, D. Yang, Z. Song, L. Xu, W. Chu, Q. Gong, and Y. Li, Polarization-controlled color-tunable holograms with dielectric metasurfaces, Optica **4**, 1368 (2017).

[22] W. Wan, J. Gao, and X. Yang, Full-color plasmonic metasurface holograms, ACS Nano **10**, 10671 (2016).

[23] K. Wakunami, P. Y. Hsieh, R. Oi, T. Senoh, H. Sasaki, Y. Ichihashi, M. Okui, Y. P. Huang, and K. Yamamoto, Projection-type see-through holographic three-dimensional display, Nat. Commun. **7**, 1 (2016).

[24] P. A. Blanche, A. Bablumian, R. Voorakaranam, C. Christenson, W. Lin, T. Gu, D. Flores, P. Wang, W. Y. Hsieh, M. Kathaperumal *et al.*, Holographic three-dimensional telepresence using large-area photorefractive polymer, Nature (London) **468**, 80 (2010).

[25] M. Campbell, D. Sharp, M. Harrison, R. Denning, and A. Turberfield, Fabrication of photonic crystals for the visible

spectrum by holographic lithography, Nature (London) **404**, 53 (2000).

[26] X. Wang, J. F. Xu, H. M. Su, Z. H. Zeng, Y. L. Chen, H. Z. Wang, Y. K. Pang, and W. Y. Tam, Three-dimensional photonic crystals fabricated by visible light holographic lithography, Appl. Phys. Lett. **82**, 2212 (2003).

[27] Y. C. Cheng, A. Isoyan, J. Wallace, M. Khan, and F. Cerrina, Extreme ultraviolet holographic lithography: Initial results, Appl. Phys. Lett. **90**, 023116 (2007).

[28] S. Larouche, Y. Tsai, T. Tyler, N. M. Jokerst, and D. R. Smith, Infrared metamaterial phase holograms, Nat. Mater. **11**, 450 (2012).

[29] X. Ni, A. V. Kildishev, and V. M. Shalaev, Metasurface holograms for visible light, Nat. Commun. **4**, 2807 (2013).

[30] N. V. Bloch, K. Shemer, A. Shapira, R. Shiloh, I. Juwiler, and A. Arie, Twisting Light by Nonlinear Photonic Crystals, Phys. Rev. Lett. **108**, 233902 (2012).

[31] A. Shapira, R. Shiloh, I. Juwiler, and A. Arie, Two-dimensional nonlinear beam shaping, Opt. Lett. **37**, 2136 (2012).

[32] A. Shapira, I. Juwiler, and A. Arie, Nonlinear computer-generated holograms, Opt. Lett. **36**, 3015 (2011).

[33] X. H. Hong, B. Yang, C. Zhang, Y. Q. Qin, and Y. Y. Zhu, Nonlinear Volume Holography for Wave-Front Engineering, Phys. Rev. Lett. **113**, 163902 (2014).

[34] B. Yang, X. H. Hong, R. E. Lu, Y. Y. Yue, C. Zhang, Y. Q. Qin, and Y. Y. Zhu, 2D wave-front shaping in optical superlattices using nonlinear volume holography, Opt. Lett. **41**, 2927 (2016).

[35] D. Wei, C. Wang, X. Xu, H. Wang, and M. Xiao, Efficient nonlinear beam shaping in three-dimensional lithium niobate nonlinear photonic crystals, Nat. Commun. **10**, 4193 (2019).

[36] S. Liu, K. Switkowski, C. Xu, J. Tian, and Y. Sheng, Nonlinear wavefront shaping with optically induced three-dimensional nonlinear photonic crystals, Nat. Commun. **10**, 3208 (2019).

[37] H. Liu, J. Li, X. Fang, X. Zhao, Y. Zheng, and X. Chen, Dynamic computer-generated nonlinear-optical holograms, Phys. Rev. A **96**, 023801 (2017).

[38] H. Liu, X. Zhao, H. Li, Y. Zheng, and X. Chen, Dynamic computer-generated nonlinear optical holograms in a non-collinear second-harmonic generation process, Opt. Lett. **43**, 3236 (2018).

[39] O. Gayer, Z. Sacks, E. Galun, and A. Arie, Temperature and wavelength dependent refractive index equations for MgO-doped congruent and stoichiometric LiNbO$_3$, Appl. Phys. B **91**, 343 (2008).

[40] See Supplemental Material at http://link.aps.org/supplemental/10.1103/PhysRevA.102.063505 for the movie.

[41] M. M. Fejer, G. A. Magel, and E. Lim, Quasi-phase-matched interactions in lithium niobate, Proc. SPIE **1148**, 213 (1990).